AGU PUBLICATIONS

JGR

Journal of Geophysical Research: Space Physics

RESEARCH ARTICLE
10.1002/2017JA024845

Key Points:
- Eclipse-generated in situ gravity waves were detected in the ionosphere
- Clear presence of waves with dominant periodicities of 25–30 min was observed around eclipse maximum
- The wave amplitudes decreased away from path of totality

Correspondence to:
C. Nayak,
cknayak@gmu.edu

Citation:
Nayak, C., & Yiğit, E. (2018). GPS-TEC observation of gravity waves generated in the ionosphere during 21 August 2017 total solar eclipse. *Journal of Geophysical Research: Space Physics, 123*, 725–738. https://doi.org/10.1002/2017JA024845

Received 1 OCT 2017
Accepted 29 NOV 2017
Accepted article online 5 DEC 2017
Published online 4 JAN 2018

GPS-TEC Observation of Gravity Waves Generated in the Ionosphere During 21 August 2017 Total Solar Eclipse

Chinmaya Nayak[1] and **Erdal Yiğit**[1]

[1] Department of Physics and Astronomy, Space Weather Lab, George Mason University, Fairfax, VA, USA

Abstract The present work investigates ionospheric effects of the 21 August 2017 total solar eclipse, particularly targeting eclipse-generated gravity waves in the ionosphere. Ionospheric total electron content (TEC) derived from Global Positioning System (GPS) data obtained from a number of stations located both along and across the path of eclipse totality has been utilized for this purpose. Distinct gravity wave-like signatures with wave periods around 20–90 min (with dominant peak at 25–30 min wave period) have been observed at all locations both in the path of totality and away from it. The observed gravity waves are more intense at locations closer to the path of totality, and the wave amplitudes decrease gradually with increasing distance from the path of totality. Our result highlights the manifestation of eclipse-generated waves in the variability of the terrestrial ionosphere.

Plain Language Summary During an eclipse, the Moon casts its shadow on the surface and atmosphere of Earth, generating exotic atmospheric behaviors, such as wave generation in the atmosphere-ionosphere system. The present paper discusses such gravity waves generated in the Earth's ionosphere during the recent 21 August 2017 eclipse which covered the entire North American continent with the eclipse totality crossing from the west to east coast. The observed gravity waves are more intense at locations closer to the path of totality, and the wave amplitudes decrease gradually with increasing distance from the path of totality.

1. Introduction

On 21 August 2017 the United States of America (USA) has experienced one of the most spectacular total solar eclipses. Over the land, the path of eclipse totality extended from the West Coast of U.S. to the East Coast over a period of a few hours. Therefore, it has been referred to as the "Great American Eclipse" in the literature to highlight its rareness. The last eclipse of similar spectacularity that stretched across North America was on 8 June 1918, crossing the U.S. from the Pacific to Atlantic, that is, during a period when the World War I was still continuing, much of the ionospheric physics was not established, and the satellite technology had yet not been invented.

During an eclipse, the moon casts its shadow on the surface and atmosphere of Earth, generating exotic atmospheric behaviors, such as wave generation in the atmosphere-ionosphere system, which this paper is going to report on. Thus, the total solar eclipse of 21 August is important from the scientific point of view since it provides an opportunity to study the variability of the ionosphere induced by waves during such rare phenomena. The path of the eclipse totality covered the entire longitudinal extent of the North American continent starting from the East Coast and ending beyond the West Coast as shown in Figure 1 by the black line.

The ionosphere is the partially ionized plasma environment of Earth's atmosphere, and it coexists with the much denser thermosphere. Its detailed structure and evolution are controlled by solar and geomagnetic processes from above (Yiğit et al., 2016) and meteorological processes from below (Yiğit & Medvedev, 2015). The ionosphere is dynamically and chemically tightly coupled to the neutral thermosphere, which is influenced greatly by gravity waves of lower atmospheric origin (e.g., Hickey & Cole, 1988; Vadas, 2007; Yiğit & Medvedev, 2010; Yiğit et al., 2009, 2012; Yua et al., 2009).

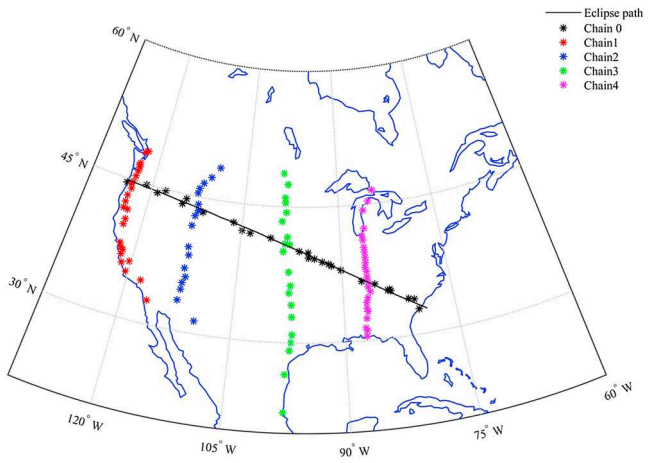

Figure 1. Map shows the path of the eclipse (solid black) and the location of the GPS stations (marked with asterisk) used in this study.

In the ionosphere there are free electrons and ions generated primarily by photoionization by solar UV and EUV radiations. During the period of an eclipse event, the direct solar illumination is reduced and thus the photoionization goes down, modulating the ionospheric structure.

The ionospheric effects caused due to solar eclipses have been studied extensively for a long time using various measurement techniques (Evans, 1965a; 1965b, Farges et al., 2001; Klobuchar & Whitney, 1965; Nayak et al., 2012; Oliver & Bowhill, 1974; Salah et al., 1986; Rishbeth, 1968) along with modeling efforts (Le et al., 2008). To a large extent, ionospheric effects in terms of changes in electron density in various layers of the ionosphere have been well characterized. However, waves generated during solar eclipses are characterized to a lesser extent. As Chimonas and Hines (1970) suggested, during a solar eclipse, the Moon's shadow moves across the atmosphere acting as a localized heat sink traveling along the path of the eclipse. This results in a localized cooling of the atmosphere in a very sharp boundary region, which in turn acts as a source of gravity waves in various regions of the atmosphere. Numerous modeling efforts have been undertaken to predict such behaviors. For example, Fritts and Luo (1993) suggested that the reduced ozone heating during a solar eclipse will generate waves which can further propagate into the upper atmosphere and thermosphere. Müller-Wodarg et al. (1998) modeled the in situ eclipse-generated effects in the thermosphere-ionosphere system using the Coupled Thermosphere-Ionosphere Plasmasphere Model (CTIP). A brief discussion of acoustic-gravity waves in the ionosphere during solar eclipses is given in the work by Knizova and Mosna (2011). There has been some observational evidence for the eclipse-generated gravity waves as well (Altadill et al., 2001; Chen et al., 2011; Manju et al., 2014; Sauli et al., 2007), which will be discussed in our paper. However, there is still limited knowledge in the characteristics of eclipse-generated gravity waves. This is also due to the reason that the general understanding of gravity wave dynamics in the ionosphere itself is largely not well established.

A part of the motivation for the present study comes from the fact that a total solar eclipse is a rare astronomical event and to be able to study this event with coordinated measurements is even rarer. As the paths of the different total eclipses are often different from each other, it could be challenging from a measurement point of view to have a full observational coverage. Because Earth's surface is 75% covered by oceans, there is a smaller chance of capturing total eclipses by ground-based instruments. As the number of observational facilities and missions are increasing, it becomes increasingly exciting to be able to better characterize solar eclipse events. In the present study, we have taken advantage of the large number of GPS (Global Positioning System) measurements at various locations both along and even across the path of the total eclipse in order to characterize possible in situ generated gravity waves in the ionosphere.

The structure of the paper is as follows. Section 2 introduces the GPS data used in this study, section 3 describes the geomagnetic conditions during the period of the eclipse, section 4 presents the large-scale response of the ionosphere to the eclipse, and section 5 presents the associated gravity wave observations. Discussion of the analysis and scientific conclusions are presented in sections 6 and 7, respectively.

2. Data and Methodology

This study predominantly utilizes GPS (Global Positioning System)-derived TEC (total electron content) data to detect any possible gravity wave generated in the ionosphere due to the solar eclipse. The TEC is a proxy for the total number of free electrons through a column of unit cross section along the line of sight between the satellite and the receiver.

$$\mathrm{TEC} = \int_{\text{receiver}}^{\text{satellite}} n_e(s)\mathrm{d}s, \tag{1}$$

where $n_e(s)$ is the electron density. The TEC measured this way is generally termed as the slant TEC which can be converted to vertical TEC by using a standard mapping function (Mannucci et al., 1993). The TEC is generally measured in TEC units where 1 total electron content unit, TECU = 10^{16} el m^2. GPS-TEC data have been used in this study for two main reasons: First, it is purely due to the availability of large number of GPS stations along and across the eclipse path in the North American sector. No other measurements cover the eclipse path

Table 1
Details of Stations in Chain 0

Station code	Latitude (deg)	Longitude (deg)	Chain #	T_S (UT)	T_M (UT)	T_E (UT)	Obscuration (%)	Station code	Latitude (deg)	Longitude (deg)	Chain #	T_S (UT)	T_M (UT)	T_E (UT)	Obscuration (%)
p386	44.40	241.03	0	16.07	17.27	18.6	100	corv	44.58	236.69	0	16.08	17.29	18.62	100
p376	44.94	236.89	0	16.08	17.30	18.62	100	p063	44.92	239.05	0	16.11	17.35	18.69	100
p386	44.40	241.03	0	16.14	17.39	18.74	100	p394	44.83	242.20	0	16.16	17.42	18.78	100
p351	43.87	245.28	0	16.20	17.49	18.88	100	idch	44.51	245.77	0	16.22	17.51	18.89	100
idif	43.51	247.94	0	16.25	17.56	18.96	100	idbb	43.48	247.95	0	16.25	17.56	18.96	100
idir	43.40	248.70	0	16.26	17.58	18.99	100	wyrf	42.83	253.67	0	16.37	17.73	19.15	100
p042	42.05	255.08	0	16.40	17.77	19.21	100	nesc	41.82	256.33	0	16.43	17.81	19.25	100
nebb	41.48	259.49	0	16.53	17.95	19.39	100	negi	40.92	261.67	0	16.57	17.99	19.44	100
neyk	40.84	262.40	0	16.59	18.02	19.46	100	nepc	40.11	263.84	0	16.63	18.08	19.52	100
mosv	39.95	265.15	0	16.67	18.12	19.57	100	mopl	39.38	265.21	0	16.68	18.13	19.58	100
morm	39.27	266.07	0	16.70	18.16	19.61	100	mobo	38.93	267.22	0	16.74	18.21	19.65	100
momk	38.68	268.11	0	16.77	18.24	19.69	100	modr	38.46	268.53	0	16.79	18.26	19.70	100
mosg	37.93	269.86	0	16.84	18.32	19.76	100	tn33	36.55	272.68	0	16.95	18.44	19.87	100
tn32	36.39	273.59	0	16.98	18.48	19.90	100	tn24	36.13	274.50	0	17.02	18.51	19.93	100
ncrb	35.32	276.20	0	17.09	18.59	20.00	100	ncbc	35.37	276.49	0	17.10	18.60	20.01	100
frkn	35.19	276.60	0	17.11	18.61	20.01	100	cola	34.08	278.87	0	17.21	18.71	20.10	100
scsr	33.92	279.65	0	17.24	18.74	20.12	100	scha	32.77	280.07	0	17.28	18.78	20.16	100

Note. T_S = eclipse start time, T_M = eclipse maximum time, T_E = eclipse end time.

as comprehensively as the GPS stations do, both spatially and temporally. Second, the higher sampling rate of the GPS data (30 s in our case) provides an excellent opportunity to more accurately detect short-period gravity waves with wave periods varying from 15 min to 1 h, which overall play an important role for ionospheric variability. Also, the effectiveness of the GPS-TEC data in detecting gravity waves in the ionosphere has been validated by numerous studies related to earthquake-generated acoustic-gravity waves in the ionosphere (e.g., Astafyeva et al., 2009, 2013; Reddy & Seemala, 2015; Rolland et al., 2011).

The GPS data used in this study have been obtained from NOAA's (National Oceanic and Atmospheric Administration) National Geodetic Survey (NGS) stations. The GPS data files themselves can be downloaded from the ftp site ftp://geodesy.noaa.gov/cors/. The GPS stations have been chosen both along and across the eclipse path in order to verify both spatial and temporal variation of any eclipse-generated gravity waves. As shown in Figure 1, the stations across the path have been divided into four different longitudinal chains which are subsequently referred to as Chains (1–4) throughout the text. The stations along the path of the totality have been termed as Chain 0, and the same terminology is used throughout the paper. The location of all the GPS stations used in the study has been shown in Figure 1, along with the eclipse path seen along the black line. The corresponding coordinates along with the eclipse timings for each station belonging to Chains 0 and 1–4 have been mentioned in Tables 1 and 2, respectively.

The ionospheric vertical TEC for each station is calculated using both code and phase measurements of the L_1 (f_1 = 1575.42 MHz) and L_2 (f_2 = 1227.60 MHz) frequencies, which effectively eliminates the contributions of clock errors and the tropospheric water vapor (Sardón & Zarraoa, 1997). The differential satellite biases and receiver biases are removed to get the absolute values of TEC (Valladares et al., 2009). Only the measurements with elevation angles higher than 20° are considered. The obtained TEC data were sampled at 30 s interval. The small period waves were extracted from the raw data by using the Hilbert-Huang Transformation (HHT) technique (Huang et al., 1998). The HHT essentially consists of two parts: (i) empirical mode decomposition (EMD) and (ii) calculation of Hilbert spectrum. The EMD decomposes the data into different orthogonal components known as intrinsic mode functions (IMFs). Afterward, the IMFs are analyzed using Hilbert transformation to calculate corresponding instantaneous wave amplitudes and frequencies. An example of empirical mode decomposition (EMD) is shown in Figure 2. TEC from pseudo-random number (PRN) 2 over

Table 2
Details of Stations in Chains 1–4

Station code	Latitude (deg)	Longitude (deg)	Chain #	T_S (UT)	T_M (UT)	T_E (UT)	Obscuration (%)	Station code	Latitude (deg)	Longitude (deg)	Chain #	T_S (UT)	T_M (UT)	T_E (UT)	Obscuration (%)
sedr	48.52	237.77	1	16.16	17.36	18.65	88.51	whd6	48.31	237.30	1	16.15	17.34	18.63	89.36
twhl	47.01	237.07	1	16.12	17.33	18.63	94.14	grmd	46.79	236.97	1	16.12	17.32	18.63	94.96
p420	46.58	237.13	1	16.12	17.32	18.63	95.70	p446	46.11	237.10	1	16.11	17.32	18.63	97.39
jime	45.52	237.00	1	16.10	17.31	18.63	99.39	p376	44.94	236.89	1	16.08	17.30	18.62	100
corv	44.58	236.69	1	16.08	17.29	18.62	100	lpsb	44.05	236.90	1	16.07	17.29	18.62	99.29
rsbg	43.23	236.64	1	16.06	17.28	18.61	96.39	p368	42.50	236.61	1	16.05	17.27	18.61	93.64
p154	41.80	236.63	1	16.04	17.26	18.61	90.99	ybhb	41.73	237.28	1	16.05	17.28	18.63	90.82
p341	40.65	237.39	1	16.04	17.27	18.63	86.67	p339	40.03	237.33	1	16.03	17.26	18.62	84.27
ohln	38.00	237.72	1	16.02	17.25	18.62	76.44	zoa2	37.54	237.98	1	16.03	17.26	18.63	74.68
mhcb	37.34	238.35	1	16.03	17.27	18.64	73.97	p210	36.81	238.26	1	16.03	17.26	18.63	71.91
p173	35.94	238.70	1	16.03	17.27	18.64	68.62	p300	36.30	239.72	1	16.05	17.30	18.68	70.29
p516	35.10	239.61	1	16.05	17.29	18.67	65.59	zla1	34.60	241.91	1	16.09	17.36	18.75	64.38
potr	32.61	243.40	1	16.13	17.40	18.80	57.34	mtms	48.54	250.31	2	16.36	17.64	18.97	84.01
p049	47.34	249.09	2	16.32	17.60	18.96	88.92	mtdt	46.58	248.00	2	16.29	17.57	18.93	92.23
mthc	45.93	247.48	2	16.27	17.56	18.93	94.85	p045	45.38	247.38	2	16.26	17.55	18.93	96.87
iddu	44.17	247.76	2	16.25	17.56	18.95	100	idif	43.51	247.94	2	16.25	17.56	18.96	100
idpo	42.86	247.56	2	16.23	17.55	18.96	98.67	p057	41.75	247.37	2	16.22	17.54	18.96	94.51
p105	39.38	247.49	2	16.21	17.54	18.97	85.62	p009	38.47	247.77	2	16.21	17.55	18.99	82.28
fred	36.98	247.50	2	16.20	17.54	18.98	76.34	gces	36.04	247.87	2	16.21	17.55	19.00	72.92
fern	35.34	247.54	2	16.21	17.54	18.99	69.98	azps	34.60	247.53	2	16.21	17.54	18.99	67.15
azbk	33.36	247.37	2	16.21	17.54	18.98	62.28	her2	31.39	250.07	2	16.31	17.62	1.904	47.30
ndmu	48.66	261.16	3	16.61	17.92	19.25	76.15	ndco	47.44	261.88	3	16.61	17.94	19.30	79.61
ndel	46.00	261.47	3	16.59	17.94	19.32	84.88	sdab	45.45	261.58	3	16.59	17.95	19.33	86.65
sdhu	44.37	261.75	3	16.58	17.96	19.36	90.22	sdpl	43.38	261.16	3	16.56	17.95	19.37	94.23
neal	41.67	262.01	3	16.58	18.00	19.43	99.12	negi	40.92	261.67	3	16.57	17.99	19.44	100
neyk	40.84	262.40	3	16.59	18.02	19.46	100	nerc	40.07	261.48	3	16.56	18.00	19.45	99.42
ict5	37.78	262.37	3	16.59	18.05	19.53	92.59	okpr	36.27	262.67	3	16.61	18.09	19.57	87.52
okdt	35.49	262.49	3	16.61	18.09	19.58	84.44	okar	34.16	262.83	3	16.64	18.12	19.61	80.06
zfw1	32.83	262.93	3	16.66	18.15	19.64	75.32	txc2	30.87	263.02	3	16.70	18.19	19.68	68.39
lcsm	30.00	262.87	3	16.71	18.20	19.68	65.05	txcu	29.13	262.72	3	16.72	18.21	19.69	61.62
txrv	26.49	262.21	3	16.77	18.24	19.69	51.71	tamp	22.27	262.13	3	16.93	18.33	19.71	37.35
mils	46.48	275.63	4	17.00	18.34	19.63	68.48	micx	45.31	274.73	4	16.97	18.33	19.65	73.03
mimn	44.37	273.83	4	16.95	18.32	19.66	76.96	mish	42.38	273.73	4	16.94	18.36	19.72	83.29
inlp	41.58	273.30	4	16.93	18.36	19.74	86.37	inwn	41.07	273.39	4	16.94	18.37	19.75	87.87
infr	40.27	273.46	4	16.94	18.39	19.78	90.35	inhc	39.75	273.47	4	16.95	18.41	19.80	92.05
iuco	39.17	273.49	4	16.95	18.41	19.82	93.86	inpa	38.56	273.50	4	16.96	18.43	19.83	95.78
intc	38.06	273.37	4	16.96	18.43	19.85	97.54	kyrr	37.60	273.49	4	16.96	18.45	19.86	98.73
kytc	36.9	273.52	4	16.97	18.46	19.88	100	tn33	36.55	272.68	4	16.95	18.44	19.87	100
tn38	35.89	273.55	4	16.99	18.49	19.91	100	tn25	35.36	273.81	4	17.00	18.51	19.93	99.32
gtac	34.71	273.34	4	16.99	18.51	19.94	96.73	alcu	34.17	273.15	4	16.99	18.51	19.95	94.72
al30	33.53	273.14	4	17.00	18.53	19.97	92.58	al35	33.16	273.24	4	17.01	18.54	19.98	91.51
alse	32.44	272.98	4	17.02	18.55	19.99	88.70	alre	31.41	272.76	4	17.03	18.56	20.01	84.85
aleb	31.09	272.94	4	17.04	18.58	20.02	84.06	pcla	30.46	272.81	4	17.05	18.59	20.03	81.74

Note. T_S = eclipse start time, T_M = eclipse maximum time, T_E = eclipse end time.

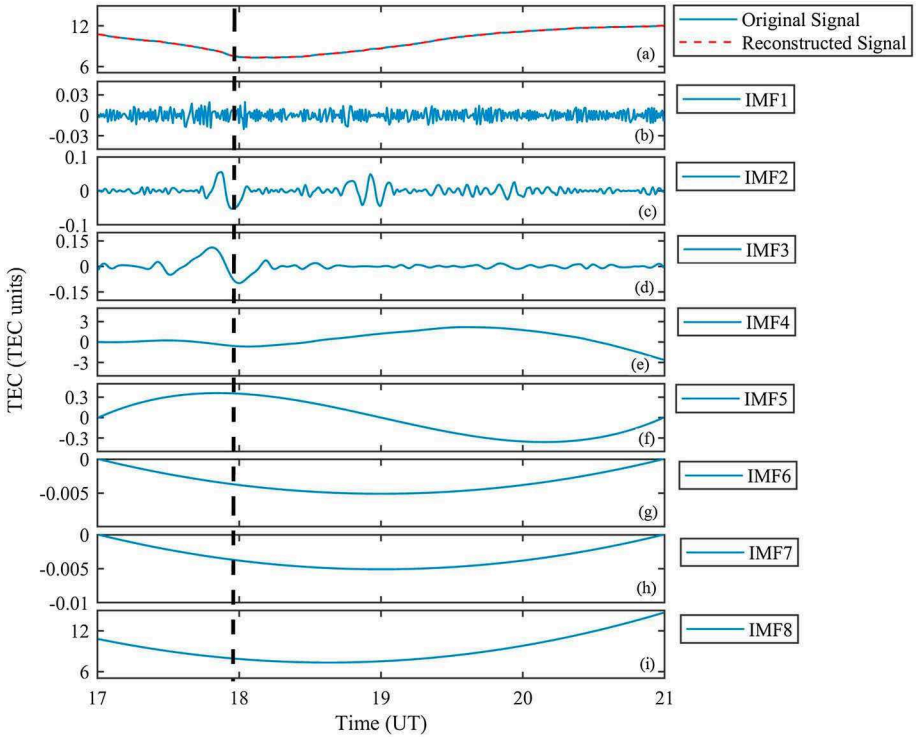

Figure 2. Empirical mode decomposition of a signal. (a) The original signal (blue solid curve). (b–i) The various IMFs (IMF 1 to IMF 8) obtained through empirical mode decomposition. The reconstructed signal (sum of all IMFs) is shown in red dashed curve in Figure 2a (plotted over the original signal.)

GPS station NEGI (latitude = 40.92°N, longitude = 261.67°) has been plotted in blue solid curve in Figure 2a. It has been decomposed to different IMFs using EMD, and the IMFs are plotted and shown in Figures 2b–2i. The vertical dashed line in each subplot shows the time of eclipse maximum. The reconstructed signal, which is the sum of all IMFs, is plotted in Figure 2a in red dashed curve. It can be observed that the IMFs (3–8) (Figures 2e–2i) mostly represent the long-term variations and the overall trend. At the same time, IMF 1 (Figure 2b) represents the highest frequency noise which is present throughout the duration of the data. Only IMF 2 (Figure 2c) and IMF 3 (Figure 2d) represent the shorter period waves that are of interest in this study. Hence, the sum of both these IMFs (IMF 2 + IMF 3) has been used as the extracted wave which is shown in Figure 5e, for this particular case. The same technique is used to extract the gravity waves from all data. Hereafter, the sum (IMF 2 + IMF 3) is termed as *high-frequency IMF component* and the same terminology is used throughout the paper for consistency.

It should be mentioned here that each GPS satellite is marked by a unique PRN (pseudo-random number). In this study, the data from PRNs 2 and 6 are specifically chosen to detect gravity waves since these two PRNs were observed by all the GPS locations during the passage of the eclipse. Although a couple of other PRNs also showed wave-like signatures, the data were either not available at all locations or it did not cover all the concerned time duration. So we have focused on data from PRNs 2 and 6 throughout this paper.

The data for eclipse path and the respective eclipse timings for each location have been obtained from NASA's https://eclipse2017.nasa.gov/sites/default/files/interactive_map/index.html.

3. Geomagnetic Conditions

The geomagnetic conditions during 20–22 August 2017 are shown in Figure 3. Figure 3 (top, middle, and bottom) plots the *SYM-H*, *Ap* index, and the *Kp* index, respectively. It should be noted that both 20 and 22 August 2017 showed mild geomagnetic activity. *SYM-H* reached a minimum of −46 nT on 20 August. Similar activity can be seen in terms of *Ap* and *Kp* indices during the first half of both 20 and 22 August. The eclipse day (21 August) was relatively quiet in terms of geomagnetic activity.

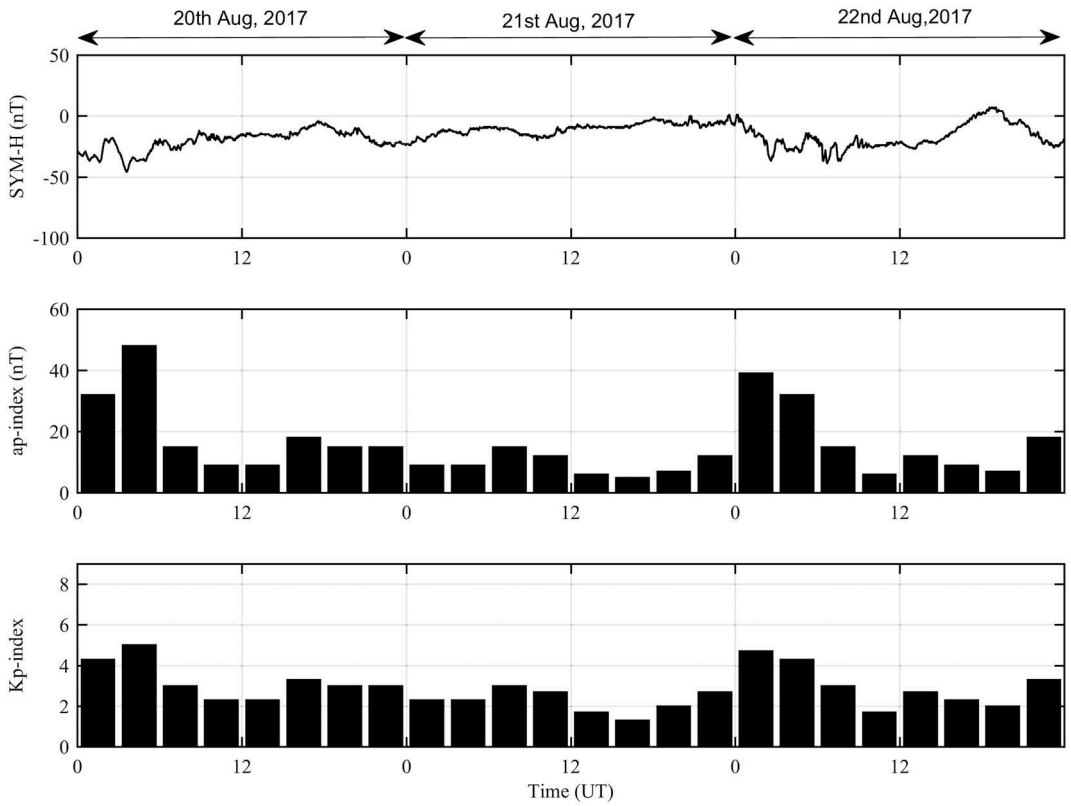

Figure 3. Geomagnetic conditions during 20–22 August 2017. The (top) *SYM-H*, (middle) *Ap* index, and (bottom) the *Kp* index, respectively.

4. Large-Scale Ionospheric Response

Before going into details of small-scale short-period gravity wave response during the eclipse, it is important to understand the large-scale ionospheric response during the eclipse. Figure 4 shows the variation of 1 min averaged TEC representing 18 different locations along the path of the eclipse (Chain 0) as shown in Figure 1. There are more than 18 stations along the path of the totality that have been utilized in this study. But the overall responses at other stations show similar behavior as the representative ones. Each panel represents the TEC variation at respective GPS stations as a function of time (UT). The green, red, and blue curves in each panel represent the TEC values for 20, 21, and 22 August 2017, respectively. The blue, red, and black vertical dashed lines represent the time of beginning, maximum, and end of eclipse at each location, respectively.

Most of the locations show clear decrease in TEC values after the eclipse onset then reach a minimum around the eclipse maximum and then gradually recover. A similar behavior was predicted in the work by Huba and Drob (2017). In the observations, however, the decrease does not perfectly coincide with the start of the eclipse. Instead, there seems to be a small time lag. Similar is the case for the minimum TEC values. The TEC attains a minimum not at the maximum eclipse but few minutes afterward. The reason for such a lag comes due the delayed response of the F_2 layer to the eclipse. It should be noted that the maximum contribution to vertical TEC comes from the F_2 layer where the electron concentration peaks (denoted by N_mF_2). The F_2 layer is influenced both by chemical and dynamical (transport) processes. The electron density maximizes at the altitude (h_mF_2) where the chemical and diffusion time constants are similar to each other, that is, $\tau_C \approx \tau_D \approx H^2/D_a$ where H represents the scale height and D_a represents the coefficient of ambipolar diffusion. The life times of the ions (electrons) in the F_2 layer are much higher as compared to those in E or F_1 layer. As a result, the E and F_1 layer responses to the eclipse are almost immediate, whereas F_2 layer response is delayed as shown in previous studies (Adeniyi et al., 2007; Nayak et al., 2012). That is the reason the TEC response in Figure 4 shows a lag between the eclipse maximum and the TEC minimum. Also, a closer look shows slight enhancement in TEC at most of the locations, once the eclipse ends.

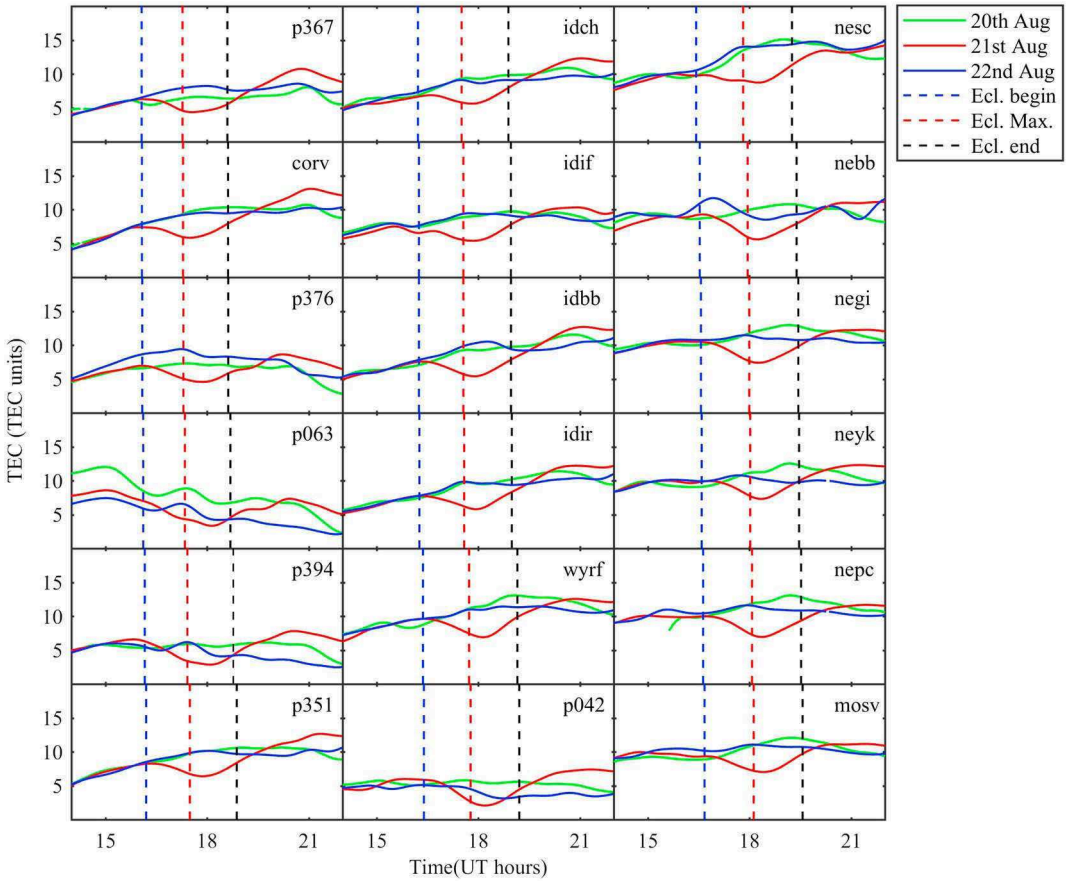

Figure 4. Ionospheric response at various GPS locations along the path of the eclipse totality. Each panel represents the TEC variation at respective GPS station as a function of time (UT). The green, red, and blue curves in each panel represent the 1 min averaged vertical TEC for 20, 21, and 22 August, 2017, respectively. The blue, red, and black vertical dashed lines represent the time of beginning, maximum, and end of eclipse at each location. A clear dip in TEC can be seen on 21 August (eclipse day) around the time of eclipse maximum. Afterward, a slight enhancement can be observed at most of the locations, once the eclipse ends.

There is a fair possibility of presence of geomagnetic disturbance effects during this duration. However, for all the 3 days, during 12–24 UT, the geomagnetic activity was fairly low as can be seen from all three parameters in Figure 3. However, all geomagnetic effects during these periods cannot be entirely ruled out.

5. Gravity Wave Observations

Figure 5 shows a comparison of any possible wave activity on 20–22 August 2017 as seen from PRN 2 over GPS station NEGI (latitude = 40.92°N, longitude = 261.67°. Figures 5a–5c represent the TEC from PRN 2 plotted as a function of time, for the respective days. Figures 5d–5f represent the high-frequency IMF component (IMF 2 + IMF 3). Figures 5g–5i show the FFT (fast Fourier transform) amplitude spectrum as a function of wave period for the respective high-frequency IMF components. Figures 5j–5l show the Hilbert spectrum representing the variation of instantaneous wave frequency with respect to time, making it easier to identify the dominant frequency at any particular time. The red vertical line represents the time of eclipse maximum on 21 August 2017. A clearly visible wave activity can be seen around the time of the eclipse maximum around 18:00 UT. Although relatively smaller waves can be observed on both 20 and 22, the wave amplitude is much stronger on 21 around the eclipse maximum. This is evident from the high-frequency IMF component (Figure 5e) and the Hilbert spectrum (Figure 5k) as well. The periodicity of the waveform, in this case, shows a peak around 25–30 min as seen from the FFT spectrum (Figure 5h) with contributions from slightly higher periods. The spectrum substantially spreads across 20–90 min showing significant contribution from waves of higher periodicities. Although the FFT can give us information about the dominant frequency/time period, it cannot give any information regarding the instantaneous frequencies. The instantaneous frequencies

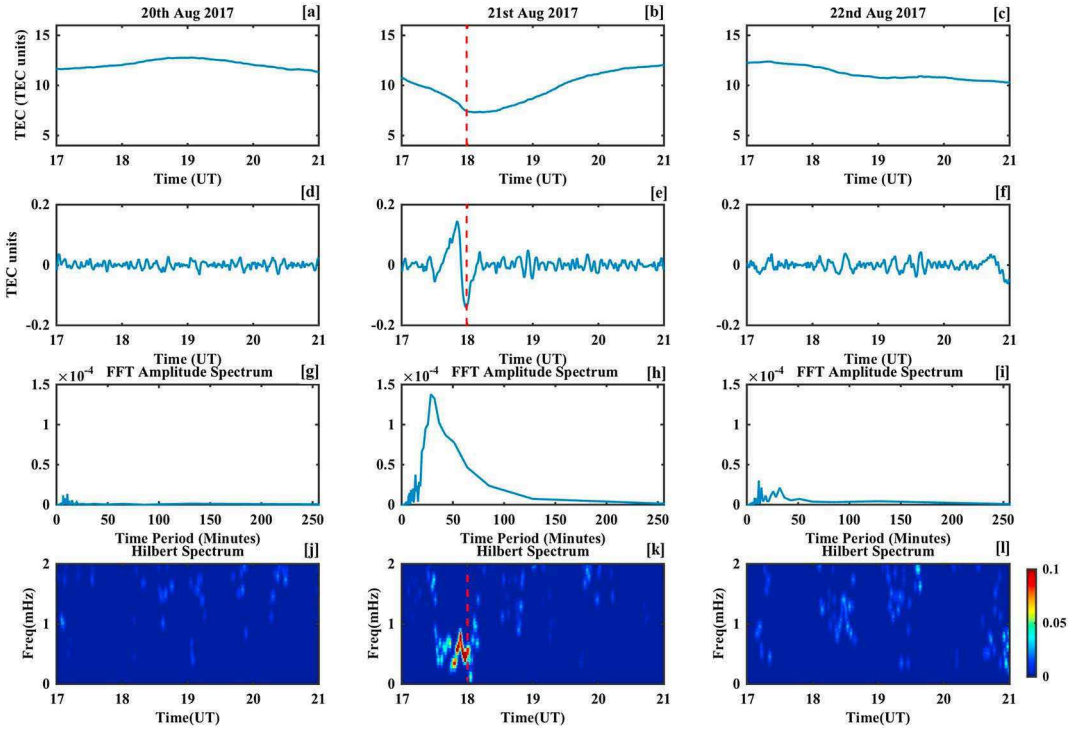

Figure 5. The figure compares the wave activity as seen over GPS station "NEGI" on (a, d, g, j) 20, (b, e, h, k) 21, and (c, f, i, l) 22 August 2017, respectively. Figures 5a–5c represent the TEC from PRN 2 for the respective days. Figures 5d–5f represent the high-frequency IMF component (IMF 2 + IMF 3). Figures 5g–5i show the FFT amplitude spectrum as a function of wave period (minutes) for the respective high-frequency IMF component. Figures 5j–5l show the Hilbert spectrum representing the variation of wave frequency with respect to time making it easier to identify the dominant frequency at any particular time.

corresponding to the wave activity can be seen from the Hilbert spectrum (Figure 5k). Clear presence of waves with frequencies 0.3–0.9 mHz (time periods ~ 20–55 min) with maximum power around 0.5 mHz (~30 min) can be seen close to the eclipse maximum, in the Hilbert spectrum. The Hilbert spectrum in this case has been calculated using the Hilbert-Huang transform (HHT) (Huang et al., 1998).

To make sure that the eclipse-generated wave detected above is not an isolated case and the wave activity is observed throughout all locations along the path of the totality, a stack plot of the high-frequency IMF components from all 34 stations along the path of the eclipse totality (Chain 0) is shown in Figure 6. The *x* axis shows time in UT. The TEC in this case is calculated from PRN 2. Figures 6a–6c represent data from 20, 21, and 22 August, respectively. It is to be noted that each location experienced an eclipse obscuration of 100%. The time of totality at each location is represented as a red dot on each curve in Figure 6b. A clear, short-period, wave-like structure can be observed on each curve around the red dot in Figure 6b indicating that the gravity wave signatures were present at all locations along the path of the totality. At the same time, it must be noted that the wave structure is predominantly centered around the red dot implying that the eclipse acts as a source for this particular wave. As a result, the waveform moves spatially along with the totality of the eclipse across the continent, from the west to east coast. However, no such coherent wave activity can be seen on the previous or next day, which further confirms the eclipse as the source/generator of the observed gravity waves.

A similar picture is shown in Figure 7 in terms of data from PRN 6 as compared to PRN 2 in Figure 6. It shows the stacked plot of high-frequency IMF components from PRN 6 for all GPS stations along the eclipse path. Similar to Figure 6, clear wave-like signatures are seen around the red dot across all stations on the eclipse day (Figure 7b). Again, such coherent structures are clearly absent on both previous (Figure 7a) and the next day (Figure 7c).

Both Figures 6 and 7 independently suggest probable gravity waves generation around the time of the eclipse maximum at each location along the path of the eclipse totality. There is, however, one more question

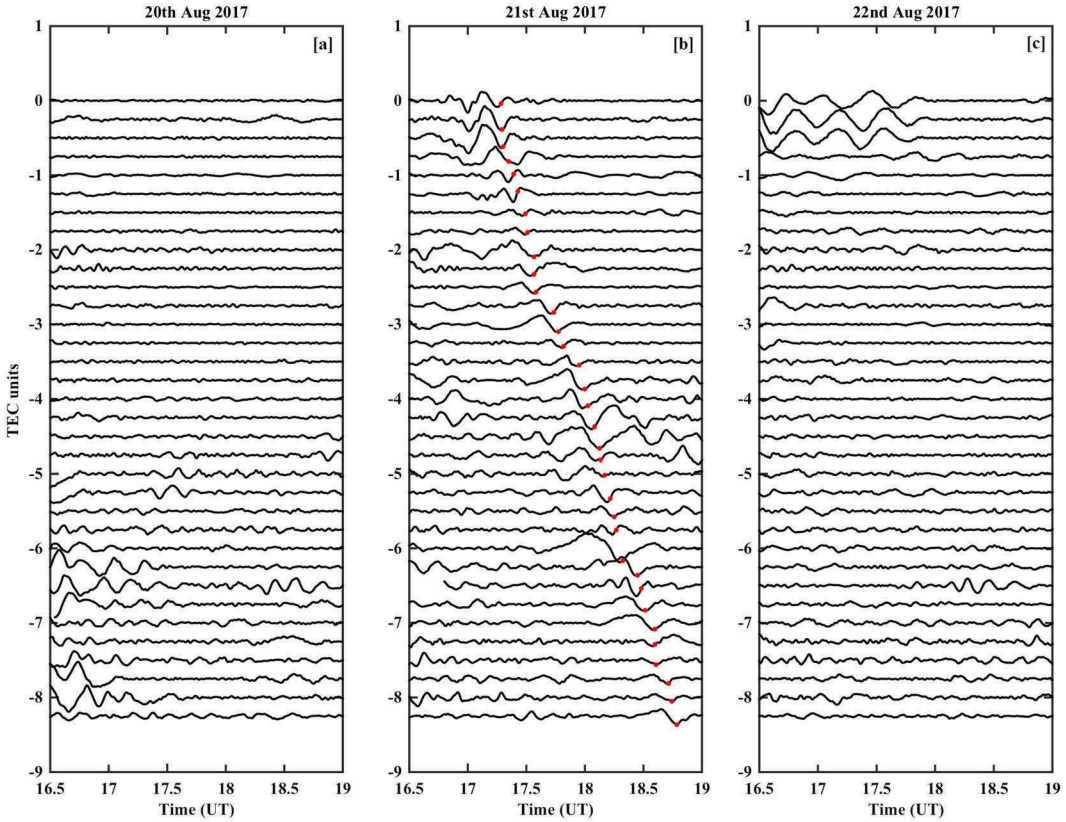

Figure 6. The figure plots the stacked high-frequency IMF components as a function of time (UT) for PRN 2 for all GPS stations taken along the path of the eclipse for (a) 20, (b) 21, and (c) 22 August 2017, respectively. The red dot on each curve in Figure 6b represents the time of maximum eclipse for each location. Clear wave structures can be seen on the eclipse day (21) around the time of eclipse maximum (red dot) moving steadily with the eclipse movement along the path. No such wave activity can be seen on the previous or next day.

that arises from Figures 6 and 7. Apart from the eclipse-generated gravity waves, both figures show wave activity at other times which is present on all 3 days. We must not forget that the ionosphere is in constant harmony with the lower atmosphere. The gravity waves generated in the lower atmosphere propagate upward reaching the ionosphere and play a major role in the dynamics of the ionosphere (Yiğit & Medvedev, 2015). The small-scale wave structures observed may possibly be the signatures of such gravity waves propagating from below. However, the eclipse-generated gravity waves clearly stand out as they move spatially with the eclipse totality.

A natural question arises about the evolution of such waves as we move away from the path of totality. If the eclipse acts as a source for the above discussed gravity waves, then the wave magnitude is expected to diminish as the eclipse magnitude decreases at locations away from the totality. To verify this hypothesis, we have used the data from stations in Chains 1 – 4 shown in Figure 1. As mentioned earlier, each of these chain of stations consists of stations both above (northward) and below (southward) the path of the eclipse totality including a couple of stations located in the path of totality. Each vertical panel in Figures 8 and 9 represents the data from each Chains 1 –4. The only difference is that Figure 8 represents data from PRN 2, whereas Figure 9 represents data from PRN 6. Each panel shows the stacked plot of high-frequency IMF components. The blue curves represent data from stations lying on the path of totality. The curves above and below the blue ones represent data from stations above and below the path of the totality, respectively. The eclipse obscuration in terms of percentage is stated above each curve. The red dots represent the time of maximum eclipse for each location. It can be clearly observed that the wave magnitude around the red dot shows a gradual decrease as we move toward locations away from 100% obscuration. As the obscuration decreases, the wave magnitude also decreases irrespective of whether the station is located above or below the path of totality. All four chains in Figures 8 and 9 show similar behavior. The decreasing amplitudes away from the blue curves further confirm that the eclipse acts as a source for these waves.

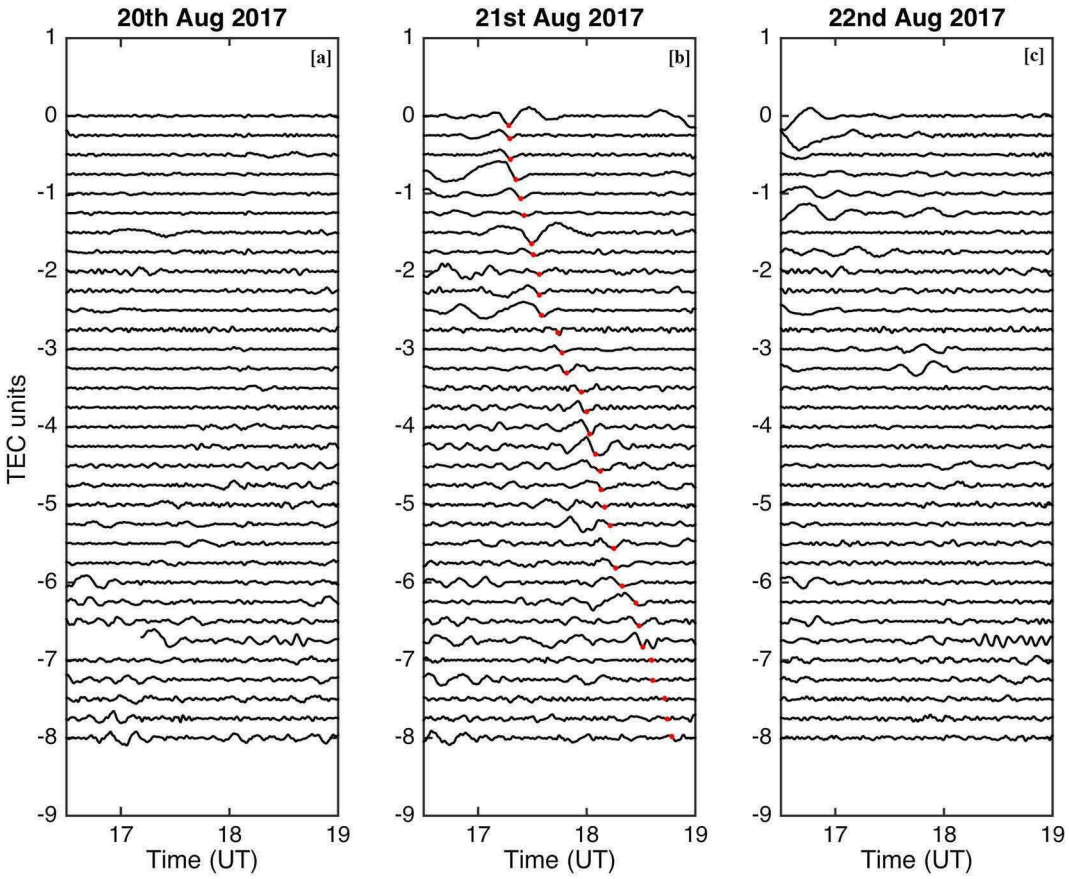

Figure 7. The figure is similar to Figure 5 but represents the stacked high-frequency IMF components as a function of time (UT) for PRN 6 for all GPS stations taken along the path of the eclipse for (a) 20, (b) 21, and (c) 22 August 2017, respectively. The red dot on each curve in Figure 7b represents the time of maximum eclipse for each location. Clear wave structures can be seen around the time of eclipse maximum (red dot) moving steadily with the eclipse movement along the path. No such wave activity can be seen on the previous or next day.

It may be argued here that the waves shown in Figures 6 and 7 may just be fluctuations moving with the forcing, which is the eclipse, in this particular case. A fluctuation can be claimed as a wave only when it starts to propagate systematically outward from the source. In this case, the eclipse acts as a forcing mechanism creating multiple gravity wave sources along its path. These gravity waves gradually propagate outward, away from the eclipse path as shown in Figures 8 and 9. A careful investigation of Figures 8 and 9 shows weaker but still distinguishable waveforms almost 30 min to 1 h after the eclipse maximum (red dot). The wave fronts are particularly evident in Figures 8d and 9d. These waves may also have contributions from the gravity waves which were generated in the lower atmosphere and have propagated to ionospheric altitudes. However, it is difficult to reach at any definitive conclusion with the present set of data since the TEC measurements provide a vertically integrated effect.

6. Discussion

Chimonas and Hines (1970) were the first to propose that a solar eclipse can act as a source for internal gravity waves in the ionosphere. The very first observational evidence came immediately afterward by Davis and da Rosa (1970). The authors showed waves with periods of around 20 min observed in columnar electron content data measured through VHF transmission from geostationary satellites ATS I and ATS III. The next observation of gravity waves during a solar eclipse came almost after two decades by Walker et al. (1991). The authors analyzed ionosonde-derived virtual height data and showed the presence of possible gravity waves with periodicities of 30–33 min. However, the amplitude spectrum also showed a secondary peak at 20–25 min which the authors neglected. In our case, the TEC values also show waves with periodicities

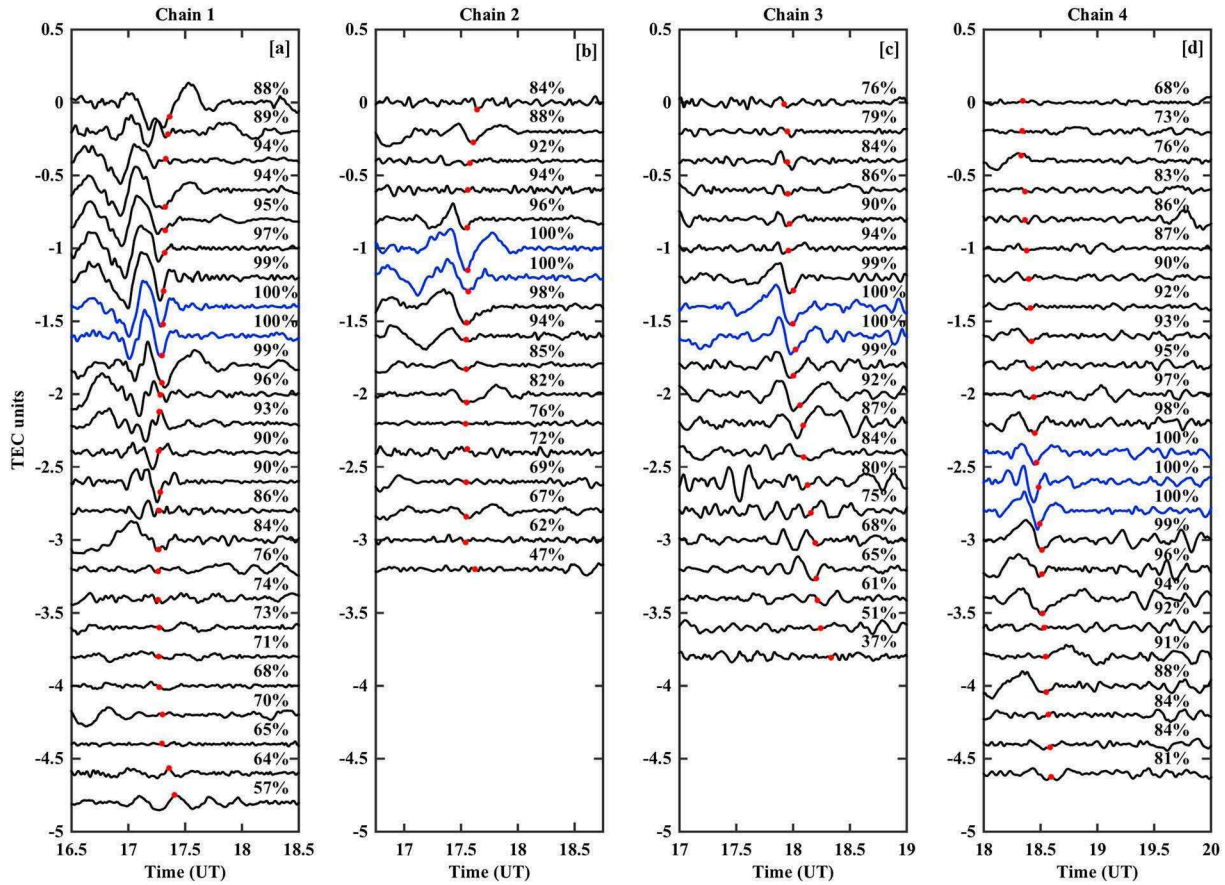

Figure 8. High-frequency IMF components as a function of time for PRN 2 for four different chains of stations across the path of the eclipse as shown in Figure 1. In each panel, the blue curves represent data from stations lying on the eclipse path (100% obscuration). The eclipse obscuration for each station is mentioned in terms of percentage above each curve. The curves above and below the blue ones represent data from stations lying above and below the path of the totality, respectively. The gradual decrease in wave amplitude can be clearly observed at stations away from the totality (decreasing eclipse obscuration).

of 20 – 25 min. Also, the maximum eclipse obscuration at the ionosonde locations in case of Walker et al. (1991) was less than 50% as opposed to 100% in our case.

There have been a few modeling studies which have attempted to predict solar eclipse-generated gravity waves in the ionosphere. Fritts and Luo (1993) proposed that the reduced ozone heating during a solar eclipse will generate waves with dominant periods of a few hours and characteristics horizontal and vertical scales of 5,000 – 10,000 km and 200 km, respectively. These waves can further propagate into the upper atmosphere and thermosphere. However, the authors did not consider any in situ generated waves at ionospheric altitudes. Müller-Wodarg et al. (1998) modeled the in situ eclipse-generated effects in the thermosphere-ionosphere system using The Coupled Thermosphere-Ionosphere Plasmasphere Model. The results showed that fluctuations in thermospheric temperature and changes in electron density propagate as waves with decreasing amplitudes, away (outward) from the path of totality. A similar behavior can be seen in Figures 8 and 9, as well. Wave amplitude gradually decreases with increasing distance from the path of totality (blue curves representing data from totality). At thermospheric/ionospheric altitudes, gravity waves are primarily dissipated by molecular diffusion, thermal conduction, and ion drag (Yiğit et al., 2008, 2009; Yiğit & Medvedev, 2017). Müller-Wodarg et al. (1998) also predicted and explained the enhancement in F_2 layer density after the eclipse in terms of enhanced O/N_2 concentration ratio. The same can be observed in terms of TEC as well as shown in Figure 4. The red curve, which represents the eclipse day TEC, clearly overtakes the green and blue curves which represent TEC on the previous and next days, respectively.

Data from ionograms have been extensively used in various studies regarding eclipse-generated gravity waves. Chen et al. (2011) studied the *Es* layer variation during a total solar eclipse and observed gravity waves with periodicities of 35 min. Similarly, Altadill et al. (2001) reported waves with periodicities of ~1 h during

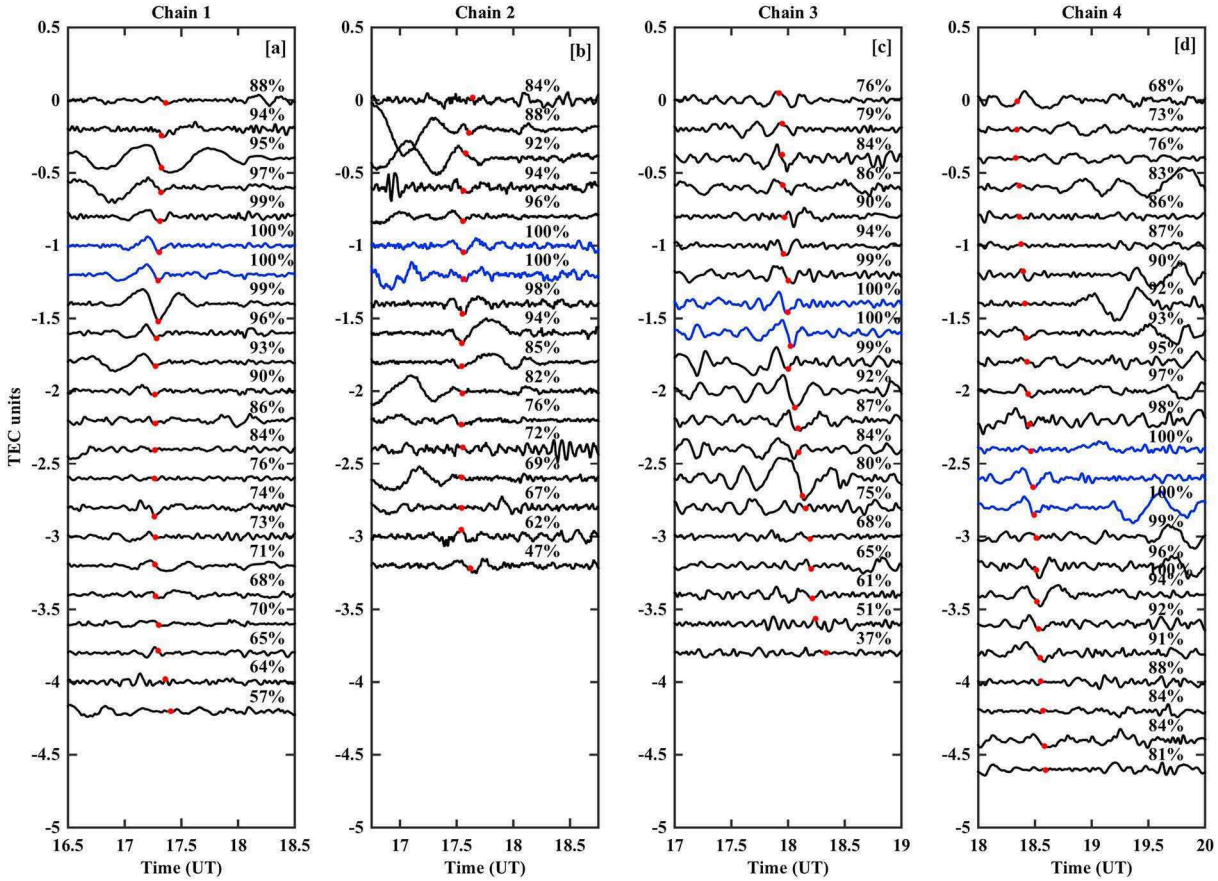

Figure 9. Similar to Figure 7 but shows high-frequency IMF components from PRN 6 for the four different chains of stations across the path of the eclipse as shown in Figure 1. In each panel, the blue curves represent data from stations lying on the eclipse path (100% obscuration). The eclipse obscuration for each station is mentioned in terms of percentage above each curve. The curves above and below the blue ones represent data from stations lying above and below the path of the totality, respectively. The gradual decrease in wave amplitude can be clearly observed at stations away from the totality (decreasing eclipse obscuration).

75% obscuration. On the other hand, Manju et al. (2014) reported wave periods of 30–100 min from f_oF_2 observations during an annular eclipse of 90% obscuration. The present study demonstrates similar wave periodicities of around 20–90 min observed in the above mentioned studies. Most of the above mentioned studies (except Chen et al., 2011, 2017) are concerned with annular eclipses, whereas we are dealing with a total solar eclipse. As in case of Chen et al. (2011), the periodicity (35 min) is closer to the peak periodicity we retrieved (25–30 min). The studies involving the data from ionosondes mostly point toward higher wave periods, the major reason being the time resolution of the data. Most of the ionosonde-derived data have time resolution of 5–15 min. However, in our case, the time resolution of GPS-TEC data is 30 s which gives us an advantage to also look at shorter period waves. Sauli et al. (2007) made an attempt to measure and characterize the acoustic-gravity waves generated in the ionosphere from ionogram data using wavelet analysis. However, the authors also emphasized the need for data with higher temporal resolution.

It is surprising that the GPS-TEC data have been scarcely used in the past to study any eclipse-driven gravity waves, considering their good spatial coverage all over the world and the high temporal resolution they provide. The very first attempt came from Jakowski et al. (2008). However, the results were inconclusive and the authors assumed that the wave amplitudes may be too small to de detected by the methods employed by them. Kumar et al. (2016) studied possible gravity waves generated during a total solar eclipse using GPS-TEC data. The authors detected presence of periodic waves of ~20–45 min and ~70–90 min periods at *F* region altitudes. However, this study was limited to data from a single GPS station. The most remarkable contribution in this regard came from Liu et al. (2011). The authors were able to detect very short period waves (<10 min) although these short period waves were detected over a few locations and absent in others. However, the present study did not find such low period waves specifically on the eclipse day.

7. Summary and Conclusions

We have studied the ionospheric effects of 21 August 2017 total solar eclipse with major focus on the eclipse-generated small-scale (low-period) gravity waves. The study utilized five chains of GPS stations with one chain along the path of the eclipse totality and four chains across the path. The major findings are as follows.

1. The TEC values at most locations decreased after the onset of the eclipse and reached a minimum value after the eclipse maximum with a small time lag. Afterward, the TEC values gradually recovered and showed an enhancement after the end of the eclipse. The results are in good agreement with past observations and modeling predictions (Huba & Drob, 2017).
2. Gravity waves with periodicities around 20–90 min (with dominant peak at 25–30 min wave period) were detected at all stations along the path of the totality. The waves were present around the time of eclipse maxima at all locations, as the waves were generated in situ with the eclipse acting as a source.
3. The gravity waves were also observed at locations away from the eclipse totality. However, the wave amplitudes clearly decreased as we moved away from the eclipse path, both in equatorward and poleward directions. The wave magnitudes decreased with decreasing eclipse magnitude. This further confirms the eclipse as the source behind the generation of such waves.
4. Further wave trains followed the above mentioned waves, with time delays of approximately 30 min to 1 h. These waves were possibly the eclipse-generated gravity waves at other locations which traveled toward the location of observation. These waves may also have contributions from the ones which were possibly generated in the lower atmosphere and propagated upward. However, such waves were embedded in the daily variations and were difficult to differentiate.

Overall, GPS-TEC measurements that aided with the Hilbert-Huang transformations provide an unprecedented view of eclipse-generated waves with good geographical coverage and excellent time resolution suitable for short-period gravity wave studies, in particular for detection and characterization.

Acknowledgments
The data supporting the figures presented in this paper can be obtained from C. N. (cnayak@gmu.edu). We would like to thank NASA's https://eclipse2017.nasa.gov/sites/default/files/interactive_map/index.html for providing the eclipse path data. We are also thankful to NOAA's (National Oceanic and Atmospheric Administration) National Geodetic Survey (NGS) for providing us the GPS-TEC data. C. N. and E. Y. were funded by the National Science Foundation (NSF) grant AGS 1452137.

References

Adeniyi, J. O., Radicella, S. M., Adimula, I. A., Willoughby, A. A., Oladipo, O. A., & Olawepo, O. (2007). Signature of the 29 March 2006 eclipse on the ionosphere over an equatorial station. *Journal of Geophysical Research*, *112*, A06314. https://doi.org/10.1029/2006JA012197

Altadill, D., Solé, J. G., & Apostolov, E. M. (2001). Vertical structure of a gravity wave like oscillation in the ionosphere generated by the solar eclipse of August 11, 1999. *Journal of Geophysical Research*, *106*, 21,419–21,428. https://doi.org/10.1029/2001JA900069

Astafyeva, E., Heki, K., Kiryushkin, V., Afraimovich, E., & Shalimov, S. (2009). Two-mode long-distance propagation of coseismic ionosphere disturbances. *Journal of Geophysical Research*, *116*, A10307. https://doi.org/10.1029/2008JA013853

Astafyeva, E., Shalimov, S., Olshanskaya, E., & Lognonne, P. (2013). Ionospheric response to earthquakes of different magnitudes: Larger quakes perturb the ionosphere stronger and longer. *Geophys Research Letters*, *40*, 1675–1681. https://doi.org/10.1002/grl.50398

Chen, G., Zhao, Z., Zhang, Y., Yang, G., Zhou, C., Huang, S., … Sun, H. (2011). Gravity waves and spread *Es* observed during the solar eclipse of 22 July 2009. *Journal of Geophysical Research*, *116*, A09314. https://doi.org/10.1029/2011JA016720

Chimonas, G., & Hines, C. O. (1970). Atmospheric gravity waves induced by a solar eclipse. *Journal of Geophysical Research*, *75*, 875–875. https://doi.org/10.1029/JA075i004p00875

Davis, M. J., & da Rosa, A. V. (1970). Possible detection of atmospheric gravity waves generated by the solar eclipse. *Nature*, *226*, 1123. https://doi.org/10.1038/2261123a0

Evans, J. V. (1965a). On the behavior of f_0F_2 during solar eclipses. *Journal of Geophysical Research*, *70*, 733–738. https://doi.org/10.1029/JZ070i003p00733

Evans, J. V. (1965b). An *F* region eclipse. *Journal of Geophysical Research*, *70*, 131–142. https://doi.org/10.1029/JZ070i001p00131

Farges, T., Jodogne, J. C., Bamford, R., Le Roux, Y., Gauthier, F., Vila, P. M., … Miro, G. (2001). Disturbances of the western european ionosphere during the total solar eclipse of 11 August 1999 measured by a wide ionosonde and radar network. *Journal of Atmospheric and Solar-Terrestrial Physics*, *63*, 915–924. https://doi.org/10.1016/S1364-6826(00)00195-4

Fritts, D. C., & Luo, Z. (1993). Gravity wave forcing in the middle atmosphere due to reduced ozone heating during a solar eclipse. *Journal of Geophysical Research*, *98*, 3011–3021. https://doi.org/10.1029/92JD02391

Hickey, M. P., & Cole, K. D. (1988). A numerical model for gravity wave dissipation in the thermosphere. *Journal of Atmospheric and Terrestrial Physics*, *50*, 689–697.

Huang, N. E., Shen, Z., Long, S. R., Wu, M. C., Shih, H. H., Zheng, Q., … Liu, H. H. (1998). The empirical mode decomposition and the Hilbert spectrum for nonlinear and non-stationary time series analysis. *Royal Society of London Proceedings*, *454*, 903–998.

Huba, J. D., & Drob, D. (2017). Sami3 prediction of the impact of the 21 august 2017 total solar eclipse on the ionosphere/plasmasphere system. *Geophysical Research Letters*, *44*, 5928–5935. https://doi.org/10.1002/2017GL073549

Jakowski, N., Stankov, S. M., Wilken, V., Borries, C., Altadill, D., Chum, J., … Cander, L. R. (2008). Ionospheric behavior over Europe during the solar eclipse of 3 October 2005. *Journal of Atmospheric and Solar-Terrestrial Physics*, *70*, 836–853. https://doi.org/10.1016/j.jastp.2007.02.016

Klobuchar, J. A., & Whitney, H. E. (1965). Ionospheric electron content measurements during a solar eclipse. *Journal of Geophysical Research*, *70*, 1254–1257. https://doi.org/10.1029/JZ070i005p01254

Knizova, P. K., & Mosna, Z. (2011). Acoustic gravity waves in the ionosphere during solar eclipse events. In M. G. Beghi (Eds.), *Acoustic Waves - From Microdevices to Helioseismology* (pp. 303–320). https://doi.org/10.5772/19722

Kumar, K. V., Maurya, A. K., Kumar, S., & Singh, R. (2016). 22 July 2009 total solar eclipse induced gravity waves in ionosphere as inferred from GPS observations over EIA. *Advances in Space Research*, *58*, 1755–1762.

Le, H., Liu, L., Yue, X., & Wan, W. (2008). The midlatitude F_2 layer during solar eclipses: Observations and modeling. *Journal of Geophysical Research*, *113*, A08309. https://doi.org/10.1029/2007JA013012

Liu, J. Y., Sun, Y. Y., Kakinami, Y., Chen, C. H., Lin, C. H., & Tsai, H. F. (2011). Bow and stern waves triggered by the Moon's shadow boat. *Geophysical Research Letters*, *38*, L17109. https://doi.org/10.1029/2011GL048805

Manju, G., Madhav Haridas, M. K., Ramkumar, G., Pant, T. K., Sridharan, R., & Sreelatha, P. (2014). Gravity wave signatures in the dip equatorial ionosphere-thermosphere system during the annular solar eclipse of 15 January 2010. *Journal of Geophysical Research: Space Physics*, *119*, 4929–4937. https://doi.org/10.1002/2014JA019865

Mannucci, A. J., Wilson, B. D., & Edwards, C. D. (1993). A New Method for Monitoring the Earth's Ionospheric Total Electron Content Using the GPS Global Network. In *Proceedings of the 6th International Technical Meeting of the Satellite Division of The Institute of Navigation (ION GPS 1993)* (pp. 1323–1332). Salt Lake City, UT.

Müller-Wodarg, I. C. F., Aylward, A. D., & Lockwood, M. (1998). Effects of a mid-latitude solar eclipse on the thermosphere and ionosphere—A modelling study. *Geophysical Research Letters*, *25*, 3787–3790. https://doi.org/10.1029/1998GL900045

Nayak, C. K., Tiwari, D., Emperumal, K., & Bhattacharyya, A. (2012). The equatorial ionospheric response over Tirunelveli to the 15 January 2010 annular solar eclipse: Observations. *Annales de Geophysique*, *30*, 1371–1377. https://doi.org/10.5194/angeo-30-1371-2012

Oliver, W. L., & Bowhill, S. A. (1974). The F_1 region during a solar eclipse. *Radio Science*, *9*, 189–195. https://doi.org/10.1029/RS009i002p00189

Reddy, C. D., & Seemala, G. K. (2015). Two-mode ionospheric response and Rayleigh wave group velocity distribution reckoned from GPS measurement following M_w 7.8 Nepal earthquake on 25 April 2015. *Journal of Geophysical Research: Space Physics*, *120*, 7049–7059. https://doi.org/10.1002/2015JA021502

Rishbeth, H. (1968). Solar eclipses and ionospheric theory. *Space Science Reviews*, *8*, 543–554. https://doi.org/10.1007/BF00175006

Rolland, L. M., Philippe, L., Elvira, A., Kherani, E. A., Kobayashi, N., Mann, M., & Hiroshi, M. (2011). The resonant response of the ionosphere imaged after the 2011 off the Pacific coast of Tohoku Earthquake. *Earth, Planets and Space*, *63*(4), 853–857. https://doi.org/10.5047/eps.2011.06.020

Salah, J. E., Oliver, W. L., Foster, J. C., Holt, J. M., & Emery, B. A. (1986). Observations of the May 30, 1984, annular solar eclipse at Millstone Hill. *Journal of Geophysical Research*, *91*, 1651–1660. https://doi.org/10.1029/JA091iA02p01651

Sardón, E., & Zarraoa, N. (1997). Estimation of total electron content using GPS data: How stable are the differential satellite and receiver instrumental biases? *Radio Science*, *32*, 1899–1910. https://doi.org/10.1029/97RS01457

Sauli, P., Roux, S., Abry, P., & Boska, J. (2007). Acoustic gravity waves during solar eclipses: Detection and characterization using wavelet transforms. *Journal of Atmospheric and Solar-Terrestrial Physics*, *69*, 2465–2484. https://doi.org/10.1016/j.jastp.2007.06.012

Vadas, S. L. (2007). Horizontal and vertical propagation of gravity waves in the thermosphere from lower atmospheric and thermospheric sources. *Journal of Geophysical Research*, *112*, A06305. https://doi.org/10.1029/2006JA011845

Valladares, C. E., Villalobos, J., Hei, M. A., Sheehan, R., Basu, S., MacKenzie, E., … Rios, V. H. (2009). Simultaneous observation of traveling ionospheric disturbances in the Northern and Southern Hemispheres. *Annales de Geophysique*, *27*, 1501–1508. https://doi.org/10.5194/angeo-27-1501-2009

Walker, G. O., Li, T. Y. Y., Wong, Y. W., Kikuchi, T., & Huang, Y. N. (1991). Ionospheric and geomagnetic effects of the solar eclipse of 18 March 1988 in East Asia. *Journal of Atmospheric and Terrestrial Physics*, *53*, 25–37. https://doi.org/10.1016/0021-9169(91)90017-2

Yiğit, E., Aylward, A. D., & Medvedev, A. S. (2008). Parameterization of the effects of vertically propagating gravity waves for thermosphere general circulation models: Sensitivity study. *Journal of Geophysical Research*, *113*, D19106. https://doi.org/10.1029/2008JD010135

Yiğit, E., Knížová, P. K., Georgieva, K., & Ward, W. (2016). A review of vertical coupling in the atmosphere-ionosphere system: Effects of waves, sudden stratospheric warmings, space weather, and of solar activity. *Journal of Atmospheric and Solar-Terrestrial Physics*, *141*, 1–12. https://doi.org/10.1016/j.jastp.2016.02.011

Yiğit, E., & Medvedev, A. S. (2010). Internal gravity waves in the thermosphere during low and high solar activity: Simulation study. *Journal of Geophysical Research*, *115*, A00G02. https://doi.org/10.1029/2009JA015106

Yiğit, E., & Medvedev, A. S. (2015). Internal wave coupling processes in Earth's atmosphere. *Advances in Space Research*, *55*(5), 983–1003. https://doi.org/10.1016/j.asr.2014.11.020

Yiğit, E., & Medvedev, A. S. (2017). Influence of parameterized small-scale gravity waves on the migrating diurnal tide in Earth's thermosphere. *Journal of Geophysical Research: Space Physics*, *122*, 4846–4864. https://doi.org/10.1002/2017JA024089

Yiğit, E., Medvedev, A. S., Aylward, A. D., Hartogh, P., & Harris, M. J. (2009). Modeling the effects of gravity wave momentum deposition on the general circulation above the turbopause. *Journal of Geophysical Research*, *114*, D07101. https://doi.org/10.1029/2008JD011132

Yiğit, E., Medvedev, A. S., Aylward, A. D., Ridley, A. J., Harris, M. J., Moldwin, M. B., & Hartogh, P. (2012). Dynamical effects of internal gravity waves in the equinoctial thermosphere. *Journal of Atmospheric and Solar-Terrestrial Physics*, *90–91*, 104–116. https://doi.org/10.1016/j.jastp.2011.11.014

Yua, Y., Hickey, M. P., & Li, Y. (2009). A numerical model characterizing internal gravity wave propagation into the upper atmosphere. *Advances in Space Research*, *44*, 836–846. https://doi.org/10.1016/j.asr.2009.05.014